Modified Robust Predictive Current Control Design of Windings-Discontinuous-Segmented PMLSM Based on an Improved Analysis Method

Anpeng Wang, Liyi Li, *Senior Member, IEEE*, and Xuzhen Huang, *Member, IEEE*

***Abstract*—A permanent magnet linear synchronous motor (PMLSM) with discontinuous-segmented windings, driven by a distributed control system, is subject to high current sampling noise and strong back-back electromotive force disturbances. Therefore, an improved robust predictive current control (RPCC) algorithm is proposed to simultaneously achieve better disturbance rejection and noise suppression performance while maintaining a suitable stability margin. First, an improved analysis method is proposed based on frequency response of a fully equivalent unity-negative feedback multi-input-multi-output (MIMO) system for comprehensive performance and stability metrics of the current closed loop. Contrary to general knowledge, for robust deadbeat predictive current control (DPCC) that combines linear extended state observer (LESO), the equivalent integrator in LESO does not reduce the deadbeat tracking characteristics of DPCC for current commands. However, as the bandwidth of LESO decreases, the excess stability margin limits the disturbance rejection and noise suppression performance of the current closed-loop system. Therefore, an improved RPCC algorithm is proposed to overcome this challenge by adding a damping term and a gain adjustment factor to the feedback controller. The correctness of the analysis method and the effectiveness of the improved control method are verified through sweep frequency experiments and time domain response experiments in a PMLSM prototype.**

***Index Terms*—Disturbance rejection, noise suppression, permanent magnet linear synchronous motor (PMLSM), robust deadbeat predictive current control (DPCC).**

Nomenclature

$\boldsymbol{u}$, $\boldsymbol{i}$	Vectors of stator voltages and currents in the dq-frame, where $\boldsymbol{u} = [u_\mathrm{d}, u_\mathrm{q}]^\mathrm{T}$, $\boldsymbol{i} = [i_\mathrm{d}, i_\mathrm{q}]^\mathrm{T}$.
$\boldsymbol{\psi}_f^s$, $\boldsymbol{\psi}_f^{\mathrm{dq}}$	Vectors of permanent magnet fluxes interlinked with a single primary winding segment in the $\alpha\beta$- and dq-frame, where $\boldsymbol{\psi}_f^s = [\psi_f^\alpha, \psi_f^\beta]^\mathrm{T}$, $\boldsymbol{\psi}_f^{\mathrm{dq}} = [\psi_f^\mathrm{d}, \psi_f^\mathrm{q}]^\mathrm{T}$.
p	Differential factor.
R_s, τ	Stator resistance and polar distance.
ω_e, θ_e	Electrical angular speed and angle, where $\theta_e = \frac{\pi(x_\mathrm{m} - x_\mathrm{m}^\mathrm{b})}{\tau}$, where x_m is the mover position.
$\hat{}$	Hat $\hat{}$ designates estimated values.
$'$	Superscript $'$ designates nominal parameters used in the controller.
$\overline{\sigma}(\cdot)$	Maximum singular value of a matrix.
$\boldsymbol{e}_i$	Error between $\boldsymbol{i}$ and $\hat{\boldsymbol{i}}$ in an observer, $\boldsymbol{e}_i = [e_i^\mathrm{d}, e_i^\mathrm{q}]^\mathrm{T} = \boldsymbol{i} - \hat{\boldsymbol{i}}$.
$\boldsymbol{I}, \boldsymbol{J}$	$\boldsymbol{I} = \begin{bmatrix} 1 & 0 \\ 0 & 1 \end{bmatrix}$, $\boldsymbol{J} = \begin{bmatrix} 0 & -1 \\ 1 & 0 \end{bmatrix}$.
$\mathcal{P}$, $\mathcal{C}$, $\mathcal{D}$	$\theta_\mathrm{e} \in \mathcal{P}$, $\mathcal{C}$, $\mathcal{D}$ means the primary is partly coupled, completely coupled, and decoupled with the secondary, respectively.

Received 18 April 2024; revised 3 July 2024 and 24 August 2024; accepted 13 October 2024. Date of publication 16 October 2024; date of current version 12 December 2024. This work was supported by the National Natural Science Foundation of China under Grant 52022040 and Grant 52277053. Recommended for publication by Associate Editor P. Mattavelli. *(Corresponding author: Liyi Li.)*

Anpeng Wang and Liyi Li are with the Department of Electrical Engineering, Harbin Institute of Technology, Harbin 150001, China (e-mail: 21b906010@stu.hit.edu.cn; liliyi@hit.edu.cn).

Xuzhen Huang is with the Department of Electrical Engineering, Nanjing University of Aeronautics and Astronautics, Nanjing 210016, China (e-mail: huangxuzhen@nuaa.edu.cn).

Color versions of one or more figures in this article are available at https://doi.org/10.1109/TPEL.2024.3482437.

Digital Object Identifier 10.1109/TPEL.2024.3482437

I. Introduction

THE moving-magnet permanent magnet linear synchronous motor (PMLSM) is essential to high-end material transmission systems [1]. It offers more freedom of motion to the mover than moving coil motors, as it eliminates the constraints of cables [2]. A segmented winding power supply is a typical driving strategy for long-distance transportation applications [3]. Two types of winding segmentation methods exist: continuous iron core segmentation [4] and discontinuous iron core segmentation [5]. The latter has advantages in terms of cost, flexibility, and diversity of application scenarios.

This article uses a distributed drive control system [6] to manipulate a windings-discontinuous-segmented PMLSM (WDS-PMLSM). The features of this motor and its drive system will be discussed in Section II. The critical challenges in controlling this system are high current sampling noise, long numerical control delay, and strong back electromotive force (EMF) disturbance, primarily affecting the current control. These challenges will be tackled in this study.

Deadbeat predictive current control (DPCC) is a widely used approach in permanent magnetic motor due to its effectiveness in compensating for numerical control delays, ease of implementation, and fast response [7], [8]. However, it cannot inherently suppress model uncertainties and disturbances. Therefore, researchers have proposed robust DPCC algorithms based on parameter identification [9], [10], disturbance observation, or both [11]. The application conditions for the former are relatively stringent because accurate parameter identification requires the

absence of other unmodeled disturbances. Most researchers have focused on the latter robust DPCC, and several observers have been proposed, including disturbance observers [12], extended state observers (ESO) [13], [14], resonant state observers [15], and sliding mode observers [16].

Ignoring the closed-loop dynamics of disturbance estimation, Wang et al. [14] studied the stability of ESO-based robust DPCC through pole migration of the closed-loop system characteristic equation but neglects noise suppression performance. Many publications investigate the balance of noise and disturbance suppression performance for observer-based robust control system. An explicit analytical solution for gain based on receding-horizon optimization is proposed in [17] to finely tune disturbance estimation and noise suppression for the nonlinear reduced-order disturbance observer. The weight coefficients in the optimization method need to be further tuned. Adding filters can further enhance the noise suppression performance of the disturbance estimation system. Apart from directly adding filters to the output measurement, a high-gain observer scheme embeds the filter inside the observer [18], but the system's stability is compromised [19]. Another technique equivalent to adding filters to enhance noise immunity is the redesign of the ESO based on augmented states. In [19], two types of third-order linear augmented ESOs are proposed to enhance the overall performance of the PMSM speed regulation system. Furthermore, a third-order nonlinear augmented nonlinear extended state observer (ESO) is proposed in [20] to enhance the robustness of the PMSM speed closed-loop system in the presence of inertia mismatch. Most studies above focus on speed or motion control systems and the balance between noise and disturbance suppression performance is investigated without giving enough consideration to the constraint of the closed-loop system's stability margin.

In other words, further research is necessary to thoroughly examine the stability margin, noise suppression performance, and disturbance rejection performance of the entire robust DPCC closed-loop system. This article improves the analysis method to facilitates the quantitative research for comprehensive performance of robust predictive current tracking system. Moreover, a modified structure of the robust predictive current controller is proposed to achieve better disturbance and noise suppression performance simultaneously while maintaining appropriate stability margins. This is a vital current control property that is crucially needed for WDS-PMLSM. The main contributions of the article are as follows:

1) The analysis method for robust DPCC is improved by further analyzing frequency response of the fully equivalent unity negative feedback multi-input-multi-output (MIMO) system. Sweep frequency experiments are conducted to verify this systematic analysis method.
2) It is revealed that excellent tracking performance of robust DPCC comes with the tradeoff of limiting the synchronous optimization of disturbance rejection and noise suppression performance.
3) From the perspective of multiperformance metric optimization, an improved robust predictive current control (RPCC) algorithm is proposed by adding a damping term and a gain adjustment factor to the feedback controller. Compared with three existing noise-immunity-enhanced robust DPCCs, the proposed modified structure shows optimal comprehensive performance in terms of stability margin, disturbance suppression, and noise immunity.

The rest of this article is organized as follows. Section II introduces the structure and characteristics of the motor and distributed drive system and then derives the mathematical model of the electrical subsystem. Section III improves the discrete MIMO frequency response analysis method based on the completely equivalent unity negative feedback system and points out the performance limitations of traditional robust DPCC. Section IV proposes and analyzes the improved robust DPCC, and compare this scheme with three existing methods comprehensively. Section V verifies the analysis method's correctness and the improved controller's effectiveness through frequency sweep and time-domain response experiments. Finally, Section VI concludes this article.

II. Motor, Drive System, and Model

The diagram in Fig. 1 illustrates the structure of WDS-PMLSM, which consists of three types of coupling between the primary and the secondary: complete coupling ($\theta_e \in \mathcal{C}$), partial coupling ($\theta_e \in \mathcal{P}$), and complete decoupling ($\theta_e \in \mathcal{D}$). The coupled permanent magnet flux exhibits significant time-varying and nonlinear characteristics for a single-segment winding, leading to nonlinear back-EMF disturbances that place higher demands on the current loop's immunity performance, as depicted in Fig. 2.

The distributed drive and control system's structure is also presented in Fig. 1. Each segmented primary is equipped with a drive unit composed of a 3-phase 3-bridge-arm voltage-source inverter (VSI) and a controller. To reduce the cost of the drive unit, the control circuit's ground is connected to the cathode of the drive circuit's dc bus. As a result, expensive isolation chips are no longer needed. The dedicated analog-to-digital conversion (ADC) chip is also discarded, and the on-chip ADC peripheral of the microcontroller unit (MCU) is used instead. However, due to these changes, it should be noted that the current sampling noise of the drive unit may be a little high, as shown in Fig. 3.

The drive units communicate through point-to-point serial communication [6]. This facilitates a smooth transition of the secondary s_i from the primary segment p_n to $p_{n\pm1}$ Specifically, a little complicated bottom calculation scheme, as shown in Fig. 4, is designed to synchronize the current of adjacent primaries so that a desired electromagnetic thrust is produced for $\theta_e \in \mathcal{P}$. However, the system's calculation architecture hinders the implementation of computation delay reduction techniques [21], [22], and a one-beat delay in the duty cycle update is inevitable.

The dq-axis current dynamics of a PMLSM can be expressed as follows, accounting for the asymmetric characteristics of its three-phase inductance and no-load flux [23]:

$$\begin{cases} p\boldsymbol{i} = \bar{\boldsymbol{A}}\boldsymbol{i} + \bar{\boldsymbol{B}}(\boldsymbol{u} - \bar{\boldsymbol{d}} + \boldsymbol{\epsilon}) \\ p\boldsymbol{\psi}_f^{\mathrm{dq}} = -\omega_e \boldsymbol{J}\boldsymbol{\psi}_f^{\mathrm{dq}} + \bar{\boldsymbol{d}} \end{cases} \tag{1}$$

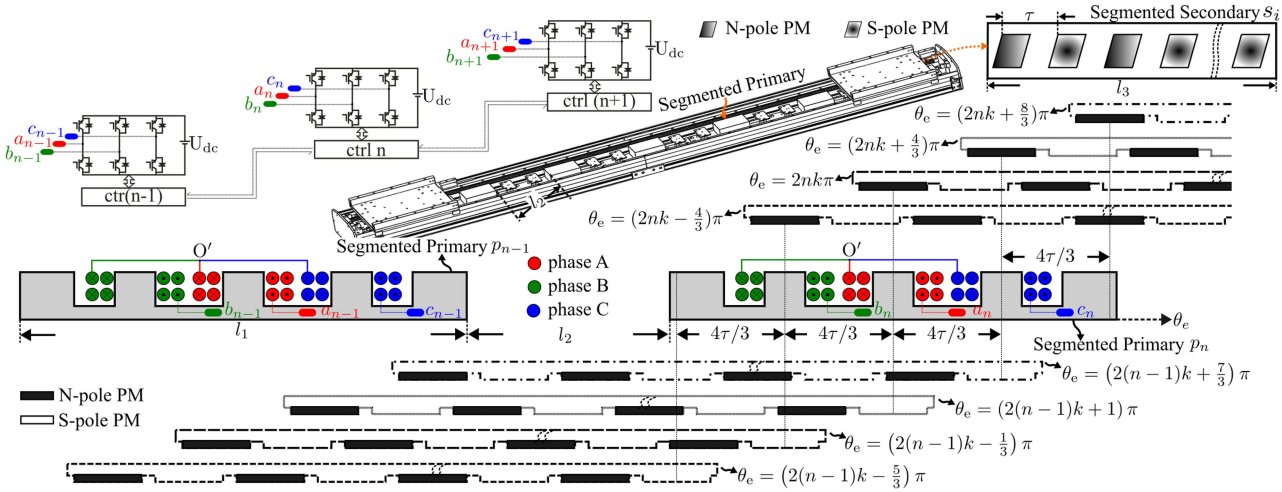

Fig. 1. Schematic diagram of the quadrupole three-slot WDS-PMLSM's structure and the distributed drive control system. The segmented primary, identified by a serial number n, is partly coupled with the secondary when $\theta_e \in ((2(n-1)k - \frac{5}{3})\pi, (2(n-1)k + \frac{7}{3})\pi) \cup ((2nk - \frac{4}{3})\pi, (2nk + \frac{8}{3})\pi) \in \mathcal{P}$. On the other hand, when $\theta_e \in ((2(n-1)k + \frac{7}{3})\pi, (2nk - \frac{4}{3})\pi) \in \mathcal{C}$, the primary winding is fully coupled with the secondary. In the remaining interval, the primary winding is fully decoupled from the secondary, i.e., $\theta_e \in \mathcal{D}$. The parameter k is determined by the secondary length l_3. Furthermore, l_1 represents the length of the segmented primary, while l_2 represents the distance between adjacent primary winding segments. It is worth noting that $l_3 = l_1 + l_2 = 2k\tau$ ensures that the electrical phases of all segmented primaries remain the same.

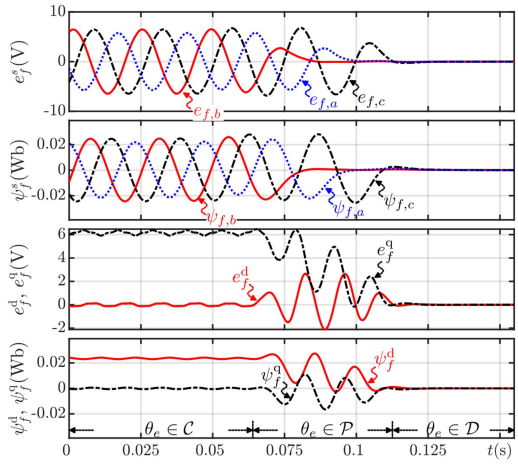

Fig. 2. Finite element simulation waveforms of no-load fluxes and back EMFs. The secondary is set as a rated speed of 1 m/s in the forward direction.

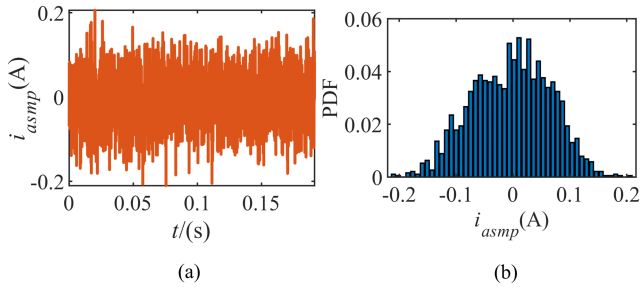

Fig. 3. Phase current sampling results at zero point. (a) Sampling waveform in time domain. (b) Probability density function (PDF).

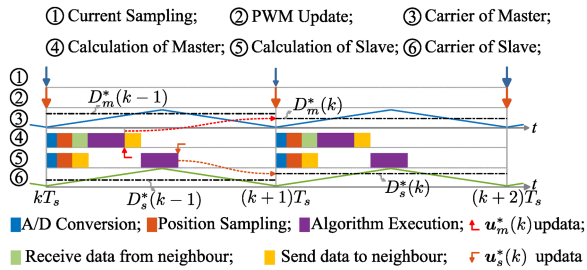

Fig. 4. Bottom real-time calculation scheme of WDS-PMLSM during the transition state ($\theta_e \in \mathcal{P}$) of vehicles.

where $\bar{\boldsymbol{A}} = -\boldsymbol{L}_s^{-1}(R_s\boldsymbol{I} + p\boldsymbol{L}_s + \omega_e\boldsymbol{J}\boldsymbol{L}_s)$; $\bar{\boldsymbol{B}} = \boldsymbol{L}_s^{-1}$; $\bar{\boldsymbol{d}} = [e_f^{\mathrm{d}}, e_f^{\mathrm{q}}]^{\mathrm{T}}$ is no-load EMFs; $\boldsymbol{\epsilon}$ is the residual unmodeled disturbances. $\boldsymbol{L}_s$ includes dq-axis self-inductance and mutual-inductance with secondary spatial harmonic due to the special asymmetric characteristics of PMLSM [24], i.e., $\boldsymbol{L}_s = \begin{bmatrix} L_{\mathrm{d}}(\theta_e) & L_{\mathrm{dq}}(\theta_e) \\ L_{\mathrm{qd}}(\theta_e) & L_{\mathrm{q}}(\theta_e) \end{bmatrix}$. As in Fig. 2, $p\psi_f^{\mathrm{dq}} \neq 0$ when $\omega_e \neq 0$.

However, accurate models for inductance and flux linkage are difficult to obtain. Based on the concept of ADRC [25], a dynamic model for current using constant parameters and lumped disturbance can be expressed as follows:

$$p\boldsymbol{i} = \boldsymbol{A}\boldsymbol{i} + \boldsymbol{B}(\boldsymbol{u} - \boldsymbol{d} - \boldsymbol{f}) \tag{2}$$

where $\boldsymbol{A} = -(R_s/L_s)\boldsymbol{I} - \omega_e\boldsymbol{J}$, $\boldsymbol{B} = (1/L_s)\boldsymbol{I}$, $\boldsymbol{d} = [0, \psi_f^v\omega_e]^{\mathrm{T}}$ is virtual no-load EMFs. The deviation between $\bar{\boldsymbol{d}}$ and $\boldsymbol{d}$ is incorporated into the lumped disturbance $\boldsymbol{f}$. L_s is the mean value of dq-axis self-inductance for $\theta_e \in \mathcal{C}$, and constant ψ_f^v is the mean value of ψ_f^{d} for $\theta_e \in \mathcal{C}$, shown in the last subgraph of Fig. 2. In the FOC strategy in this article, the angle of d-axis (i.e., θ_e) is not the angle of $\boldsymbol{\psi}_f^{\mathrm{s}}$ which is not linearly independent with the position of the secondary. An appropriate bias of θ_e ensures that the mean value of ψ_f^{q} for $\theta_e \in \mathcal{C}$ is zero, as shown as Fig. 2. The relationship between actual and constant parameters

TABLE I
PARAMETERS OF WDS-PMLSM

Symbol	Parameter	Nominal Values
L_0	Electrical Inductance	3.7 mH
R_s	Electrical Resistance	0.65 Ω
ψ_f	PM Flux	0.0225 Wb
τ	Pole Pitch	0.012 m
v_n	Nominal Velocity	1 m/s
F_n	Nominal Thrust	40 N
V_n	Nominal Voltage	12 Vpp
I_n	Nominal Current	5 A
M_m	Mover Mass	2 kg
V_{dc}	DC Link Voltage	48 V
T_s	Control period	0.1 ms

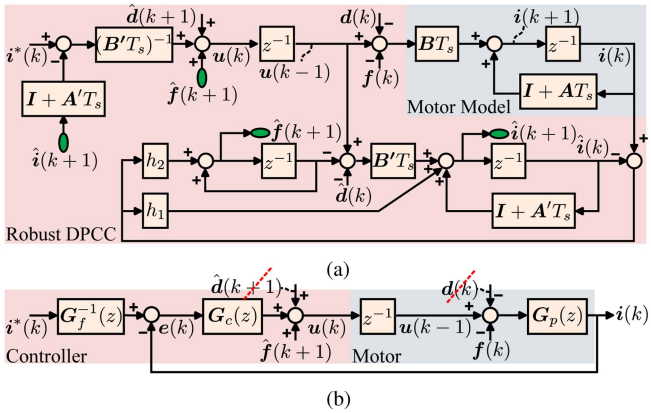

Fig. 5. (a) Structure of the traditional robust DPCC. (b) The equivalent unity-feedback system used in [14].

can be expressed as $\bar{\boldsymbol{X}} = \boldsymbol{X} + \Delta\boldsymbol{X}$, where $\boldsymbol{X}$ can be $\boldsymbol{A}$, $\boldsymbol{B}$, and $\boldsymbol{d}$. Consequently, the lumped disturbance $\boldsymbol{f}$ can be shown as $-\boldsymbol{B}^{-1}[\Delta\boldsymbol{A}\boldsymbol{i} + \Delta\boldsymbol{B}(\boldsymbol{u} - \boldsymbol{d} - \Delta\boldsymbol{d} + \boldsymbol{\epsilon})] + \Delta\boldsymbol{d} - \boldsymbol{\epsilon}$.

The inverter carrier ratio is 0.0042 at rated speed according to parameters in Table I. Therefore, using the first-order Euler method, we can discretize the current dynamics accurately. Accounting for the one-beat delay in the duty cycle update shown in Fig. 4, the current dynamics in the discrete-time domain can be expressed as follows:

$$\boldsymbol{i}(k+1) = (\boldsymbol{I} + \boldsymbol{A}T_s)\,\boldsymbol{i}(k) + \boldsymbol{B}T_s[\boldsymbol{u}(k-1) - \boldsymbol{d}(k) - \boldsymbol{f}(k)]. \quad (3)$$

III. TRADITIONAL ROBUST DPCC AND ANALYSIS

The structure of the traditional robust DPCC controller is shown in Fig. 5(a). Based on the deadbeat principle, the voltage control law shown in (4) uses the ESO-predicted current $\hat{\boldsymbol{i}}(k+1)$ and disturbance $\hat{\boldsymbol{f}}(k+1)$

$$\begin{aligned}\boldsymbol{u}(k) = {} & (\boldsymbol{B}'T_s)^{-1}\left[\boldsymbol{i}^*(k) - (\boldsymbol{I} + \boldsymbol{A}'T_s)\,\hat{\boldsymbol{i}}(k+1)\right] \\ & + \hat{\boldsymbol{d}}(k+1) + \hat{\boldsymbol{f}}(k+1) \end{aligned} \quad (4)$$

where $\hat{\boldsymbol{d}}(k+1) \approx \hat{\boldsymbol{d}}(k) = [0,\ \psi_f^{v\prime}\omega_e(k)]^{\mathrm{T}}$ is the direct estimation of virtual no-load flux. The reasons of approximation for $\hat{\boldsymbol{d}}$ in adjacent current control periods are twofolds. First, $\psi_f^{v\prime}$ is the nominal value of constant virtual no-load flux, thus $\psi_f^{v\prime}$ is also constant. Second, the electrical time constant is much smaller than the mechanical time constant [26].

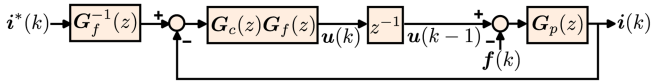

Fig. 6. Completely equivalent unity-feedback system. Compared to Fig. 5(b), it further considers the close-loop dynamics from $\boldsymbol{u}$, $\boldsymbol{i}$ to $\hat{\boldsymbol{f}}$.

The ESO expands the current $\boldsymbol{i}$ and disturbance $\boldsymbol{f}$ into a new state $\boldsymbol{X} = [\boldsymbol{i}, \boldsymbol{f}]^{\mathrm{T}}$, whose dynamics can be expressed as

$$\hat{\boldsymbol{X}}(k+1) = \boldsymbol{S}_{x,x}\hat{\boldsymbol{X}}(k) + \boldsymbol{S}_{u,x}\left[\boldsymbol{u}(k-1) - \hat{\boldsymbol{d}}(k)\right] + \boldsymbol{H}\boldsymbol{e}_i(k) \quad (5)$$

where $\boldsymbol{S}_{x,x} = \begin{bmatrix} \boldsymbol{I} + \boldsymbol{A}'T_s & -\boldsymbol{B}'T_s \\ 0 & \boldsymbol{I} \end{bmatrix}$, $\boldsymbol{S}_{u,x} = [\boldsymbol{B}'T_s,\ 0]^{\mathrm{T}}$, $\boldsymbol{H} = [h_1\boldsymbol{I},\ h_2\boldsymbol{I}]^{\mathrm{T}}$. The feedback gain can be determined according to the bandwidth-parameterization method, $h_1 = 2\omega_{oc}T_s$ and $h_2 = -\omega_{oc}^2 T_s L_s'$ [15].

A. Traditional Analysis Method

Let $\hat{\boldsymbol{i}}'(z) = \mathcal{Z}[\hat{\boldsymbol{i}}(k+1)]$ and $\boldsymbol{u}'(z) = \mathcal{Z}[\boldsymbol{u}(k-1)]$. According to the block diagram of ESO in Fig. 5(a), the closed-loop impulse transfer function of $\hat{\boldsymbol{i}}'(z)$ is as follows:

$$\hat{\boldsymbol{i}}'(z) = z\left[z\boldsymbol{I} - (\boldsymbol{I} + \boldsymbol{A}'T_s) + \boldsymbol{h}'\right]^{-1}\left\{\boldsymbol{h}'\boldsymbol{i}(z) + \boldsymbol{B}'T_s\boldsymbol{u}'(z)\right\} \quad (6)$$

where $\boldsymbol{h}' = h_1\boldsymbol{I} - \boldsymbol{B}'T_s\frac{h_2}{z-1}$. By substituting the expression mentioned above into the DPCC feedback loop, the DPCC current control system can be transformed into an equivalent unity-feedback system, as shown in Fig. 5(b). In this system, the equivalent feedback controller $\boldsymbol{G}_c$ and the equivalent feedforward controller $\boldsymbol{G}_f^{-1}$ can be expressed as follows:

$$\begin{cases} \boldsymbol{G}_p(z) = [z\boldsymbol{I} - (\boldsymbol{I} + \boldsymbol{A}T_s)]^{-1}\,\boldsymbol{B}T_s \\ \boldsymbol{G}_c(z) = (\boldsymbol{B}'T_s)^{-1}\,(\boldsymbol{I} + \boldsymbol{A}'T_s)\,(z\boldsymbol{I} + \boldsymbol{h}')^{-1}\,\boldsymbol{h}'z \\ \boldsymbol{G}_f^{-1}(z) = z^{-1}\boldsymbol{h}'^{-1}\left[z\boldsymbol{I} - (\boldsymbol{I} + \boldsymbol{A}'T_s) + \boldsymbol{h}'\right](\boldsymbol{I} + \boldsymbol{A}'T_s)^{-1}. \end{cases} \quad (7)$$

It is essential to mention that (7) is a more stringent approach than (16)–(18) of [14]. This is because matrix multiplication does not follow the commutative law, and deriving the transfer function matrix for MIMO systems requires strict adherence to specific rules [27].

In addition, the equivalent system shown in Fig. 5(b) does not consider the closed-loop dynamics of the disturbance estimate $\hat{\boldsymbol{f}}$. Wang et al. [14] assumed that $\boldsymbol{f}(z) = z^{-1}\hat{\boldsymbol{f}}'(z)$ where $\hat{\boldsymbol{f}}'(z) = \mathcal{Z}[\hat{\boldsymbol{f}}(k+1)]$, and therefore concludes that the steady-state error $\boldsymbol{e}(\infty)$ is zero. However, if this analytical method can be further improved, some of the more surprising properties of robust DPCC will be found.

B. Further Consideration for $\hat{\boldsymbol{f}}$ dynamics in Analysis

This article analyzes the performance and stability of robust DPCC based on the closed-loop impulse transfer function of $\hat{\boldsymbol{f}}'(z)$ in (8) and the fully equivalent unity-feedback system shown in Fig. 6, where the equivalent feedback controller $\boldsymbol{G}_c$ and the equivalent feedforward controller $\boldsymbol{G}_f^{-1}$ change from (7)

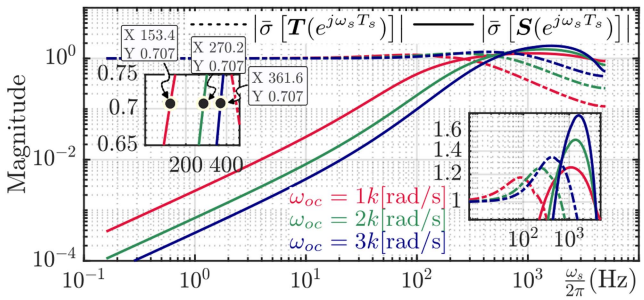

Fig. 7. Frequency response of traditional robust DPCC shown in Fig. 5(a) based on the equivalent system shown in Fig. 6. $\overline{\sigma}(\boldsymbol{S})$ in mid- and low-frequency bands shows the disturbance suppression performance, the peak values $\max_{\omega_s}\overline{\sigma}[\boldsymbol{S}(\omega_s)]$ and $\max_{\omega_s}\overline{\sigma}[\boldsymbol{T}(\omega_s)]$ represent stability margin, and $\overline{\sigma}(\boldsymbol{T})$ in the high-frequency band means noise suppression performance. In this paper, the frequency responses is analyzed in theory for the 1 m/s rated speed operation.

to (9)

$$\hat{\boldsymbol{f}}'(z) = \frac{z}{z-1}h_2\left\{\boldsymbol{I} - \left[z\boldsymbol{I} - (\boldsymbol{I} + \boldsymbol{A}'T_s) + \boldsymbol{h}'\right]^{-1}\boldsymbol{h}'\right\}\boldsymbol{i}(z) - \frac{z}{z-1}h_2\left[z\boldsymbol{I} - (\boldsymbol{I} + \boldsymbol{A}T_s) + \boldsymbol{h}'\right]^{-1}\boldsymbol{B}'T_s\boldsymbol{u}'(z) \tag{8}$$

$$\begin{cases}\boldsymbol{G}_c(z) = (\boldsymbol{B}'T_s)^{-1}\left[z\boldsymbol{I} - (\boldsymbol{I} + \boldsymbol{A}'T_s) + \boldsymbol{h}'\right]\cdot \left(z\boldsymbol{I} + \boldsymbol{h}' + \boldsymbol{B}'T_s\frac{h_2}{z-1}\right)^{-1} \\ \boldsymbol{G}_f(z) = \left[z\left(\boldsymbol{I} + \boldsymbol{A}'T_s\right) + \boldsymbol{B}'T_s\frac{z}{z-1}h_2\right]\cdot \left[z\boldsymbol{I} - (\boldsymbol{I} + \boldsymbol{A}'T_s) + \boldsymbol{h}'\right]^{-1}\boldsymbol{h}' - \boldsymbol{B}'T_s\frac{z}{z-1}h_2.\end{cases} \tag{9}$$

Fig. 6 shows that the robust DPCC can be considered a two-degree-of-freedom control system, which allows it to achieve both tracking and disturbance rejection performance. The system's complementary sensitivity transfer function $\boldsymbol{T}$ and the sensitivity transfer function $\boldsymbol{S}$ is presented in (10). It is worth noting that $\boldsymbol{T}\boldsymbol{G}_f^{-1} \equiv \boldsymbol{I}$, which means that the robust DPCC controller, designed based on deadbeat principle and active disturbance rejection techniques, can theoretically achieve the desired tracking performance with a delay of two control periods through the equivalent feedforward controller $\boldsymbol{G}_f^{-1}$. Moreover, the equivalent integrator in ESO does not impact this exceptional dynamic tracking performance.

$$\boldsymbol{i}(z) = \underbrace{\boldsymbol{G}_p z^{-1}\boldsymbol{G}_c\boldsymbol{G}_f\left(\boldsymbol{I} + \boldsymbol{G}_p z^{-1}\boldsymbol{G}_c\boldsymbol{G}_f\right)^{-1}}_{\boldsymbol{T}(z)}\boldsymbol{G}_f^{-1}\boldsymbol{i}^*(z) + \underbrace{\left(\boldsymbol{I} + \boldsymbol{G}_p z^{-1}\boldsymbol{G}_c\boldsymbol{G}_f\right)^{-1}}_{\boldsymbol{S}(z)}(-\boldsymbol{G}_p)\,\boldsymbol{f}(z). \tag{10}$$

However, theoretically perfect command tracking performance limits the other performance of robust DPCC. As illustrated in Fig. 7, the disturbance suppression performance, stability margin, and high-frequency noise suppression performance of robust DPCC are all affected by the unique parameter ω_{oc}. Suppose ω_{oc} is increased. In that case, the disturbance suppression performance in the mid-and low-frequency bands will improve overall, but this will also decrease the stability margin and high-frequency noise suppression performance.

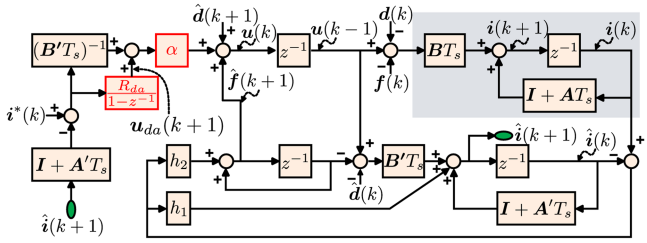

Fig. 8. Block diagram of the modified RPCC scheme.

We expect to appropriately improve the high-frequency noise suppression performance while reducing the degree of change in stability margin ($\max_{\omega_s}\overline{\sigma}[\boldsymbol{S}(\omega_s)]$), and ensuring appropriate disturbance suppression performance. That is, to unbind the synchronous variation characteristics of stability margin, high-frequency noise suppression performance, and disturbance rejection performance. In other words, the excess stability margin can be converted into a more balanced control performance (disturbance and noise suppression). To achieve this goal, further improving the structure of robust DPCC is necessary.

IV. Design and Analysis of Modified RPCC

A. Structure and Performance Analysis

The structure of further improved RPCC is shown in Fig. 8. A damping term $R_{\mathrm{da}}\boldsymbol{I}/(1-z^{-1})$ and a gain adjustment factor α are added to the feedback regulator. Based on the analysis method proposed in Section III, the structure shown in Fig. 8 can be transformed into a fully equivalent unity negative feedback system shown in Fig. 6. The equivalent feedback regulator $\boldsymbol{G}_c$ and feedforward controller $\boldsymbol{G}_f^{-1}$ are given by (11) and (12), respectively. Here, $\boldsymbol{G}_{\mathrm{lr}}$ is computed using the expression $\alpha[(\boldsymbol{B}'T_s)^{-1} + R_{\mathrm{da}}\boldsymbol{I}/(1-z^{-1})]$.

$$\boldsymbol{G}_f(z) = \left[z\left(\boldsymbol{I} + \boldsymbol{A}'T_s\right) + \boldsymbol{G}_{lr}^{-1}\frac{z}{z-1}h_2\right]\left[z\boldsymbol{I} - (\boldsymbol{I} + \boldsymbol{A}'T_s) + \boldsymbol{h}'\right]^{-1}\boldsymbol{h}' - \boldsymbol{G}_{lr}^{-1}\frac{z}{z-1}h_2 \tag{11}$$

$$\boldsymbol{G}_c(z) = (\boldsymbol{B}'T_s)^{-1}\left[z\boldsymbol{I} - (\boldsymbol{I} + \boldsymbol{A}'T_s) + \boldsymbol{h}'\right]\left\{\begin{array}{c} z\boldsymbol{I} + \boldsymbol{h}' + \frac{\boldsymbol{B}'T_s h_2}{z-1} + \\ (\boldsymbol{B}'T_s\boldsymbol{G}_{lr} - \boldsymbol{I})(\boldsymbol{I} + \boldsymbol{A}'\boldsymbol{T_s}) \end{array}\right\}^{-1}\boldsymbol{G}_{lr}\boldsymbol{B}'T_s. \tag{12}$$

Moreover, Fig. 9 shows the frequency responses of sensitivity and complementary sensitivity of the proposed RPCC close-loop system according to (10)–(12). In the first subgraph of Fig. 9, the red solid line intersects with the blue dashed line in the low- and mid-frequency range, while in the high-frequency range of the second subgraph of Fig. 9, it intersects with the green dotted line. This indicates that the improved RPCC has disturbance suppression performance comparable to that of the conventional

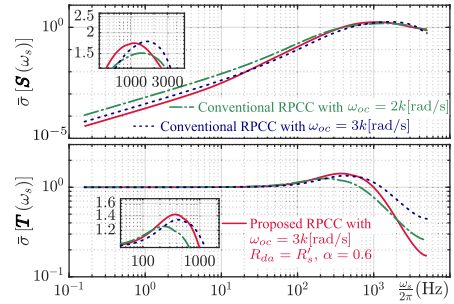

Fig. 9. Comparison between the proposed modified RPCC shown in Fig. 8 and traditional robust DPCC shown in Fig. 5(a) by frequency response.

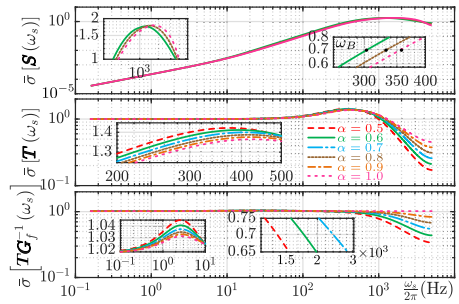

Fig. 10. Frequency responses of modified RPCC shown in Fig. 8 with $\omega_{\text{oc}} = 3000$ rad/s, $R_{\text{da}} = R'_s$ and different control parameter α.

RPCC with $\omega_{\text{oc}} = 3k$ rad/s, and high-frequency noise suppression performance comparable to that of the conventional RPCC with $\omega_{\text{oc}} = 2k$ rad/s.

Furthermore, the first subgraph of Fig. 9 shows that the peak value of the red solid line is the same as that of the blue dotted line, indicating that the improved RPCC stability margin has not changed significantly compared to the conventional RPCC with $\omega_{\text{oc}} = 3k$ rad/s. This stability margin has been shown to be an appropriate choice in [14].

It is important to note that the frequency response shown in Fig. 9, obtained from theoretical analysis, will be further verified in subsequent frequency sweep experiments. The analysis above demonstrates that the improved controller structure can further balance and adjust the disturbance rejection and high-frequency noise suppression performance while keeping the stability margin unchanged. This is a critical feature required by the WDS-PMLSM drive system, which experiences high current sampling noise and strong back EMF disturbance.

Fig. 10 shows the impact of the additional degrees of freedom α. As α changes from 0.6 to 1.0, $M_S \triangleq \max_{\omega_s} \bar{\sigma}[\boldsymbol{S}(\omega_s)]$ remains unchanged, indicating that the sensitivity of the stability margin to α is low. As α increases, the closed-loop system bandwidth ω_{B} ($\bar{\sigma}[\boldsymbol{S}(\omega_{\text{B}})] = 0.707$) increases, while the high-frequency $\bar{\sigma}[\boldsymbol{T}(\omega_s)]$ in Fig. 10 also increase, indicating that the choice of performance only occurs between disturbance and noise suppression.

It is worth noting that the conventional RPCC can also balance disturbance and noise suppression performance by adjusting the unique parameter ω_{oc} as shown in Fig. 7. However, the comprehensive performance is weaker than the proposed modified RPCC, as shown in Fig. 11. The improved RPCC can adjust the two performances to a better region by keeping the stability margin unchanged.

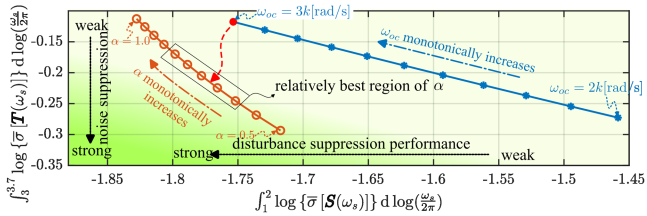

Fig. 11. Quantitative analysis of noise and disturbance suppression performance for the conventional RPCC (star-marker line) and the proposed modified RPCC (circ-marker line) with $R_{\text{da}} = R'_s$.

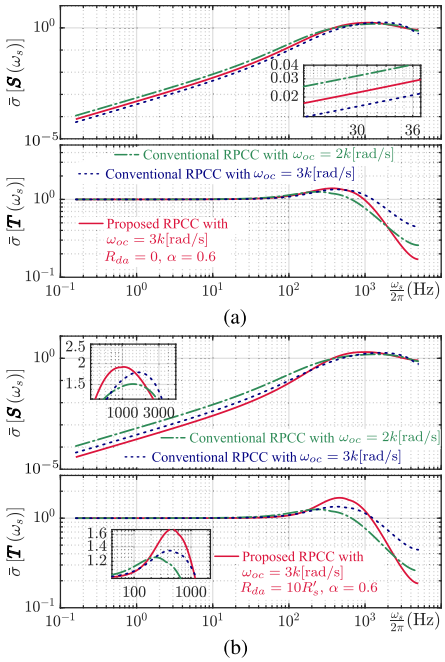

Fig. 12. Effect of different R_{da} of the modified RPCC's damping term on the current close loop system. (a) $R_{\text{da}} = 0$. (b) $R_{\text{da}} = 10R'_s$.

In addition, reducing α will sacrifice the perfect command tracking performance of the conventional RPCC, as shown in the last subgraph of Fig. 10, which is necessary to enhance the antiinterference and antinoise performance simultaneously; however, when $\alpha > 0.5$, the bandwidth of instruction tracking is greater than 1.2 kHz. Subsequent experiments have shown that this metric meets the dynamic performance requirements of the PMLSM outer loop controller for the current controller.

B. Further Discussion

1) The Effect of R_{da}: Based on the frequency response analysis method proposed in Section III, the impact of different choices of R_{da} on the current closed-loop system is shown in Fig. 12. In Fig. 12(a), R_{da} is set to zero. At low frequencies, the

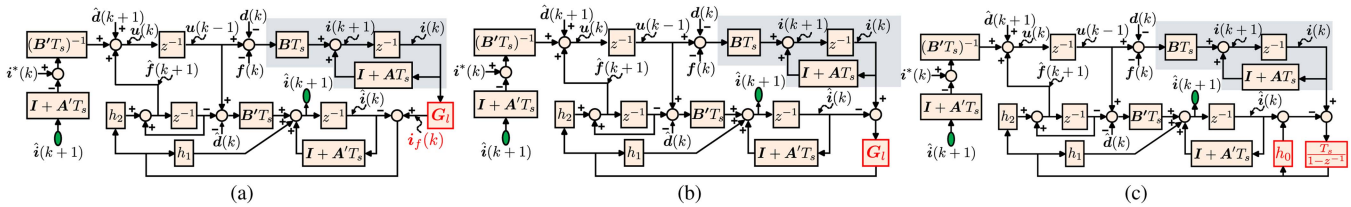

Fig. 13. Block diagrams of existing RPCCs for enhancing noise suppression based on low-pass filter (LPF). (a) The LPF-based RPCC1 with LPF outside of LESO; (b) The LPF-based RPCC2 which is the variant of the high gain observer proposed in [18]; (c) The augmented-state-based RPCC (ASRPCC) which is derived from ADRC method for speed regulation system in [19] and [20].

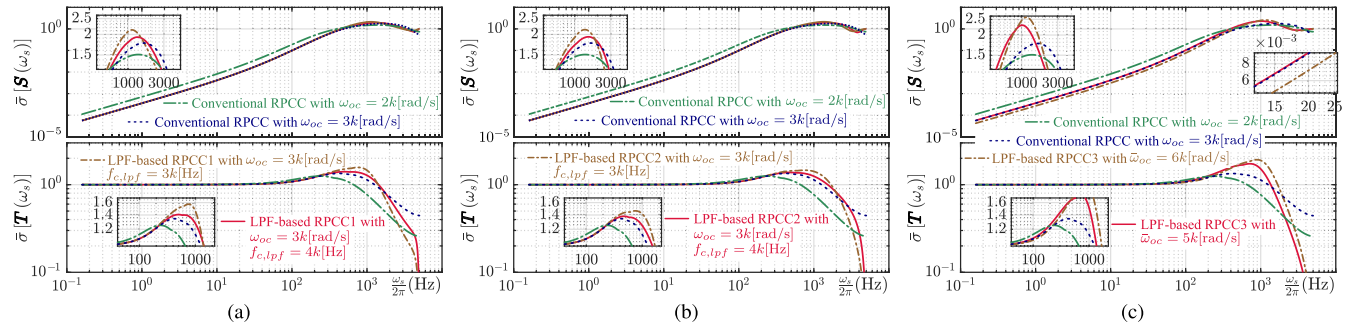

Fig. 14. Comparison between the existing RPCCs shown in Fig. 13 and the conventional RPCC shown in Fig. 5(a) by frequency response. (a) LPF-based RPCC1. (b) LPF-based RPCC2. (c) ASRPCC.

$\bar{\sigma}[\boldsymbol{S}(\omega_s)]$ of the improved RPCC lies between the two traditional RPCCs with different bandwidth parameters, indicating that the disturbance rejection performance of the improved RPCC with $R_{\rm da} = 0$ is weaker than that of the traditional RPCC with $\omega_{\rm oc} = 3k$ rad/s. In Fig. 12(b), $R_{\rm da} = 10R'_s$. At mid-to-low frequencies, the $\bar{\sigma}[\boldsymbol{S}(\omega_s)]$ of the improved RPCC is smaller than that of the traditional RPCC with $\omega_{\rm oc} = 3k$ rad/s. The M_s of the improved RPCC is close to 2, and $M_T > 1.6$ ($M_T \triangleq \max_{\omega_s} \bar{\sigma}[\boldsymbol{T}(\omega_s)]$). At high frequencies, the $\bar{\sigma}[\boldsymbol{T}(\omega_s)]$ of the improved RPCC is generally larger than that of the traditional RPCC with $\omega_{\rm oc} = 2k$ rad/s. These frequency response characteristics indicate that when $R_{\rm da} = 10R'_s$, although the low-frequency disturbance rejection performance is improved, the stability margin and noise suppression performance are weaker than those of the traditional robust DPCC. As shown in Fig. 9, when $R_{\rm da}$ is set to the nominal resistance value R'_s, the improved RPCC can achieve an optimal balance of disturbance and noise suppression performance while maintaining almost unchanged relative stability of the current closed-loop system. $R_{\rm da} = R'_s$ is a design considering that the winding resistance introduces appropriate damping to the current dynamics.

2) The Comparison With Existing Methods: Fig. 13 shows three existing robust DPCC strategies that enhance measurement noise suppression capabilities. $\boldsymbol{G}_l = \frac{b_1 z + b_0}{a_1 z + a_0}\boldsymbol{I}$, the coefficients are determined by the first order Butterworth discrete-time LPF algorithm and the cut-off frequency $f_{c,\rm lpf}$. Based on the systematic analysis method proposed in Section III, the analytical expressions of the transfer matrices in Fig. 6 for the three existing robust DPCCs are derived as (13) and (14), where (13) corresponds to LPF-based RPCC1, and (14) corresponds to LPF-based RPCC2 and ASRPCC. The $\boldsymbol{G}_c(z)$ of LPF-based RPCC1 is the same as that in (9). The frequency responses of the current closed-loop system by these transfer matrices are shown in Fig. 14.

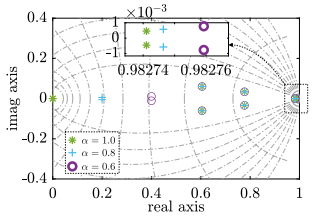

Fig. 15. Distribution of state matrix's eigenvalues of modified-RPCC-based close-loop system with $\omega_{\rm oc} = 3k$ rad/s, $R_{\rm da} = R'_s$, and different α.

The added LPF element $\boldsymbol{G}_l$ in LPF-based RPCC1 does not affect the disturbance rejection performance at low-to-mid frequencies. However, under the constraint of the stability margin limit, its noise suppression performance at high frequencies is not as good as the proposed improved RPCC. As shown by the red curve in Fig. 14(a), when the cutoff frequency $f_{c,\rm lpf}$ of $\boldsymbol{G}_l$ is set to 4 kHz, the peaks of the sensitivity and complementary sensitivity (M_S and M_T) of the LPF-based RPCC1 current closed-loop system are comparable to those of the improved RPCC shown by the red curve in Fig. 9, with $M_S < 2$, $M_T \leq 1.4$. However, for $\bar{\sigma}[\boldsymbol{T}(\omega_s)]$, the red curve in Fig. 14(a) is higher than the green dotted line at high frequencies, and the red curve in Fig. 9 crosses the green dotted line at high-frequency band, indicating that under the same stability margin, the noise suppression performance of the LPF-based RPCC1 current closed-loop system is weaker than that of the

proposed improved RPCC. As shown by the brown dotted line in Fig. 14(a), when $f_{c,\mathrm{lpf}}$ is reduced to 3 kHz, the noise suppression performance of the LPF-based RPCC1 current closed-loop system improves. However, the stability margin significantly decreases, with $M_S > 2,\ M_T \approx 1.6$

$$\boldsymbol{G}_f(z) = \left\{ \left[z\left(\boldsymbol{I} + \boldsymbol{A}'T_s\right) + \boldsymbol{B}'T_s \frac{z}{z-1} h_2 \right] \cdot \left[z\boldsymbol{I} - \left(\boldsymbol{I} + \boldsymbol{A}'T_s\right) + \boldsymbol{h}' \right]^{-1} \boldsymbol{h}' - \boldsymbol{B}'T_s \frac{z}{z-1} h_2 \right\} \boldsymbol{G}_l \quad (13)$$

$$\begin{cases} \boldsymbol{G}_f(z) = \left[z\left(\boldsymbol{I} + \boldsymbol{A}'T_s\right) + \boldsymbol{B}'T_s \frac{z}{z-1} h_2 \boldsymbol{G}_l \right] \left[z\boldsymbol{I} - \left(\boldsymbol{I} + \boldsymbol{A}'T_s\right) + \boldsymbol{h}'\boldsymbol{G}_l \right]^{-1} \cdot \boldsymbol{G}_l\boldsymbol{h}' - \boldsymbol{B}'T_s \frac{z}{z-1} h_2 \boldsymbol{G}_l \\ \boldsymbol{G}_c(z) = \left(\boldsymbol{B}'T_s\right)^{-1} \left[z\boldsymbol{I} - \left(\boldsymbol{I} + \boldsymbol{A}'T_s\right) + \boldsymbol{h}'\boldsymbol{G}_l \right] \cdot \left(z\boldsymbol{I} + \boldsymbol{h}'\boldsymbol{G}_l + \boldsymbol{B}'T_s \frac{h_2}{z-1} \boldsymbol{G}_l \right)^{-1}. \end{cases} \quad (14)$$

As shown in Fig. 14(b), LPF-based RPCC2 places $\boldsymbol{G}_l$ inside the observer, and its frequency response characteristics are similar to those of LPF-based RPCC1. Therefore, under the constraint of the stability margin limit, its noise suppression performance at high frequencies is also weaker than that of the proposed improved RPCC.

ASRPCC is equivalent with LPF-based RPCC2, with the equivalent LPF $\boldsymbol{G}_l(z) = \frac{zT_s}{(h_0T_s+1)z-1}\boldsymbol{I}$. The difference between the two control strategies is that ASRPCC can synchronously adjust the cutoff frequency of the equivalent filter $\boldsymbol{G}_l$ and the disturbance estimation dynamics based on the single parameter $\bar{\omega}_{\mathrm{oc}}$, with $h_0 = 3\bar{\omega}_{\mathrm{oc}}$, $h_1 = 3\bar{\omega}_{\mathrm{oc}}^2 T_s$, $h_2 = -\bar{\omega}_{\mathrm{oc}}^3 L_s' T_s$ [19]. The frequency responses of the closed-loop system for different $\bar{\omega}_{\mathrm{oc}}$ are shown in Fig. 14(c). When $\bar{\omega}_{\mathrm{oc}} \geq 5k$ rad/s, the disturbance rejection and noise suppression performance of the ASRPCC current closed-loop system can rival those of the improved RPCC shown in Fig. 9, but its stability margin is far weaker, with $M_S \geq 2,\ M_T > 1.6$.

In summary, the proposed improved RPCC current closed-loop system outperforms the existing three RPCCs regarding comprehensive performance in stability margin, disturbance rejection performance, and noise immunity. Moreover, it is worth noting that the above theoretical analysis will be verified by frequency sweep experiment in Section V-D.

3) Stability Analysis: Generally, the gain margin (GM) and phase margin (PM) of the open-loop transfer function in a current closed-loop system can reflect its stability. According to [27], M_S is closely related to the stability margin and can be introduced to characterize relative stability. For a given M_s, the following GM and PM can be ensured: GM $\geq \frac{M_s}{M_s-1}$, PM $\geq 2\arcsin\frac{1}{2M_s} \geq \frac{1}{M_s}$ rad. As shown in Fig. 9, the improved RPCC has $M_s \leq 1.8$, which ensures that the current closed-loop system across the entire speed range has GM ≥ 7 dB and PM $\geq 31^\circ$. In addition, the stability of the proposed improved RPCC can be verified through the state matrix of the discrete-time state space equation. The state matrix $\boldsymbol{A}_{cl}$ of the current closed-loop system based on the improved RPCC is shown in (15) shown at the bottom of this page, according to Fig. 8, Eqs. (3) and (5). Furthermore, the eigenvalue distribution under different tuning factors α is shown in Fig. 15. The eigenvalues of $\boldsymbol{A}_{\mathrm{cl}}$ are all within the unit circle, and according to Theorem 5. D4 in [28], the entire current closed-loop system is asymptotically stable.

V. Experimental Results and Discussion

A. System Setup

The entire drive system is shown in Fig. 16, so that the secondary can move across the region of $\theta_e \in \mathcal{P}$ smoothly. Fig. 17 depicts an experimental platform developed to conduct a series of experiments to verify the accuracy of the proposed analysis method and the performance and robustness of the modified RPCC. The platform comprises an WDS-PMLSM prototype with two movers and multiple segmented primaries. The PMLSM has the nominal parameter values elaborated in Table I. Each primary is equipped with a drive control unit. Each drive control unit comprises an MCU, an field programmable gate array (FPGA), and a two-level, three-phase, three-leg VSI comprising six MOSFETs. The driving platform is powered by a 48 V switching power supply that supplies the dc bus voltage. The drive control units communicate with each other via the high speed communication through the serial peripheral interface (SPI) and have successfully achieved cross-segment operation of the mover. In order to obtain the position of the mover, a linear magnetic grating scale with an accuracy of 0.2 μm is utilized. The MCU is connected to the monitoring application Jscope [29] via the debugging tool Jlink, facilitating communication between the platform and the PC.

B. Analysis Method Verification

A set of sweep frequency experiments is conducted to verify the accuracy of the analysis method based on the fully equivalent unity negative feedback system, shown in Fig. 6. A chirp signal is introduced into the *d*-axis feedback current, starting at 10 Hz and ending at 3000 Hz, and sustained for 30 s. This allows us to obtain the frequency response gains of the traditional robust DPCC sensitivity transfer and complementary sensitivity functions, as shown in Fig. 18. The frequency response gains obtained from the sweep frequency experiments are consistent with the theoretical values calculated based on (9) and (10).

$$\begin{bmatrix} \boldsymbol{i}(k+1) \\ \hat{\boldsymbol{i}}(k+1) \\ \boldsymbol{u}_{da}(k) \\ \hat{\boldsymbol{f}}(k+1) \end{bmatrix} = \underbrace{\begin{bmatrix} \boldsymbol{I} + \boldsymbol{A}T_s & -\alpha\left(\boldsymbol{B}\boldsymbol{B}'^{-1} + R_{da}T_s\boldsymbol{B}\right)\left(\boldsymbol{I} + \boldsymbol{A}'T_s\right) & \alpha T_s\boldsymbol{B} & T_s\boldsymbol{B} \\ h_1\boldsymbol{I} & \left(\boldsymbol{I} + \boldsymbol{A}'T_s\right)\left[(1-\alpha)\boldsymbol{I} - \alpha R_{da}T_s\boldsymbol{B}'\right] - h_1\boldsymbol{I} & \alpha T_s\boldsymbol{B}' & \boldsymbol{0} \\ \boldsymbol{0} & -R_{da}\left(\boldsymbol{I} + \boldsymbol{A}'T_s\right) & \boldsymbol{I} & \boldsymbol{0} \\ h_2\boldsymbol{I} & -h_2\boldsymbol{I} & \boldsymbol{0} & \boldsymbol{I} \end{bmatrix}}_{\boldsymbol{A}_{cl}} \begin{bmatrix} \boldsymbol{i}(k) \\ \hat{\boldsymbol{i}}(k) \\ \boldsymbol{u}_{da}(k-1) \\ \hat{\boldsymbol{f}}(k) \end{bmatrix} + \cdots \quad (15)$$

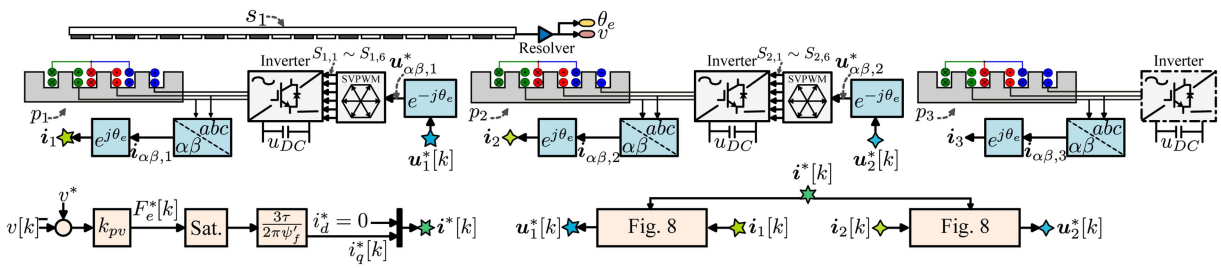

Fig. 16. Block diagram of FOC-based WDS-PMLSM drives with the modified RPCC for $\theta_e \in \mathcal{P}$ of s_1.

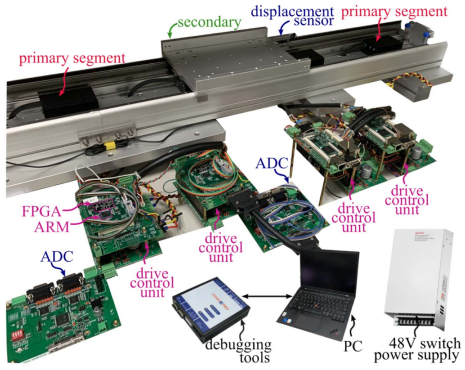

Fig. 17. Experimental setup description.

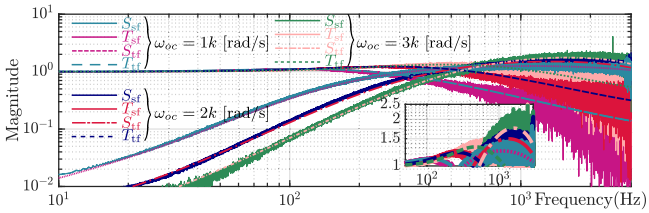

Fig. 18. Gains of $\boldsymbol{T}(z)$ and $\boldsymbol{S}(z)$ for traditional robust DPCC obtained by the frequency sweep experiments and compared with the analysis method proposed in Section III. The subscript "sf" denotes the sweeping frequency, while "tf" means the transfer function deduced in theory. Due to the chirp signal's short duration in the high-frequency range and the low signal-to-noise ratio, there is significant noise in the high-frequency band of T_{sf}.

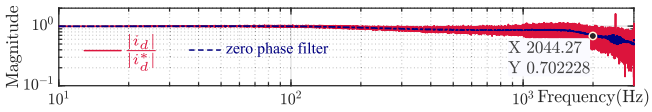

Fig. 19. Frequency response of traditional robust DPCC with $\omega_{\mathrm{oc}} = 1k$ rad/s, obtained by the sweep frequency experiment, for the command tracking.

To test the command tracking performance of the traditional robust DPCC, a chirp signal with the same properties was injected into the d-axis reference current. The value of the parameter ω_{oc} was set to a lower value of 1000 rad/s. The theoretical bandwidth ω_{B} of the current closed-loop system is approximately 154 Hz, indicating limited disturbance rejection performance, as shown in Fig. 7. However, the robust DPCC exhibits strong tracking performance, as indicated by the sweep frequency results shown in Fig. 19. The AC reference signals

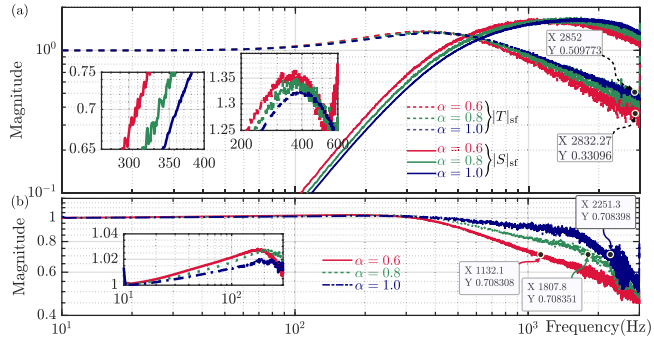

Fig. 20. Frequency response of modified RPCC, obtained by the sweeping frequency experiment with $\omega_{\mathrm{oc}} = 3000$ rad/s. (a) The gains of sensitivity and complementary sensitivity function. (b) The gain of $\boldsymbol{T}\boldsymbol{G}_f^{-1}$ in (10).

around 2 kHz have an amplitude attenuation of 0.707. Remarkably, the high-frequency disturbances introduced into the current loop by the nonlinear dead-zone voltage of the VSI prevent the sweep frequency results from fully replicating the theoretically perfect tracking performance. The robust DPCC is unable to effectively suppress these disturbances under these conditions. The result in Fig. 19 verifies the theoretical conclusion $\boldsymbol{T}\boldsymbol{G}_f^{-1} \equiv 1$ in Section III-B.

C. Modified RPCC Performance

Repeating the sweep frequency experiments with the controller replaced by the modified RPCC, the experimental results are shown in Fig. 20. In Fig. 20(a), the bandwidth ω_{B} for different values of α and the noise suppression performance at high frequencies align well with the theoretical calculations presented in Fig. 10. However, for the same reasons mentioned in Fig. 19, the sweep frequency results indicate a slightly lower bandwidth for command tracking than the theoretical values described in Fig. 10.

The effect of R_{da} is also verified by the same sweep frequency experiments shown in Fig. 21. The experiment results align with the theoretical analysis results shown in Fig. 12. Increasing R_{da} gradually increase the disturbance suppression performance at middle frequency band, but decrease the stability margin and noise immunity performance in the high frequency band.

Since $R_{\mathrm{da}} = R_s'$ is a design considering that the winding resistance introduces appropriate damping to the current dynamics, in the following experiments, R_{da} of the proposed modified

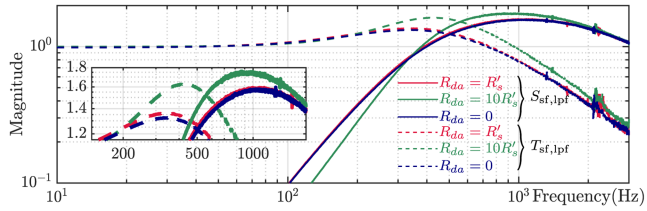

Fig. 21. Frequency response of modified RPCC, obtained by the sweeping frequency experiment with $\omega_{oc} = 3000$ rad/s, $\alpha = 0.6$ and different R_{da}. The frequency responses are processed by zero-phase filter.

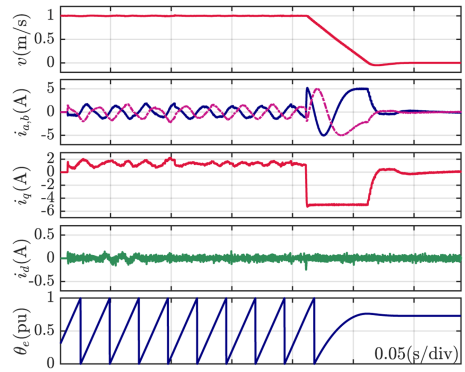

Fig. 22. Response of the modified RPCC with $\omega_{oc} = 3000$ rad/s and $\alpha = 0.6$ when speed decreases from 1 m/s to zero.

RPCC is set as R'_s. At the same time, as shown in Fig. 11, when $\omega_{oc} = 3k$ rad/s, the relatively best region of the gain adjustment factor α is [0.6,0.8] for noise immunity and disturbance suppression. As α increases, the noise immunity performance decreases. However, as shown in Figs. 10 and 20, to ensure the command tracking bandwidth exceed 1 kHz, α needs to be bigger than 0.6. Therefore, in the following experiments, α is chosen as 0.6 and $\omega_{oc} = 3k$ rad/s for the proposed modified RPCC for the sake of better noise immunity performance.

The time-domain response experiment for the current loop occurs at a rated speed of 1 m/s, as shown in Fig. 22. During the initial 0.1 s, a significant back-EMF harmonic disturbance exists for a single-segment winding during this period due to $\theta_e \in \mathcal{P}$. The d-axis disturbance amplitude is approximately 2.6 V, and the fundamental harmonic frequency is around 349 rad/s. Please note that only the time-domain waveforms of the current and voltage for a single-segment winding are presented due to space limitations.

The results of the experiment on the performance of two current prediction control algorithms for disturbance and noise suppression are presented in Fig. 23. The sum's square root of squared error (RSSE) of the d-axis current in the first phase for the four cases is defined as $\Sigma_{kT_s=t_0}^{t_0+0.1} i_d^2(kT_s)$ and recorded as 3.54, 1.70, 1.49, and 1.40 in Fig. 23(a), (b), (c), and (d), respectively. The RSSE of noise in u_d^* is defined as $\Sigma_{kT_s=t_0}^{t_0+0.05}[u_d^*(kT_s) - u_{d,\text{fir}}^*(kT_s)]^2$ where $u_{d,\text{fir}}^*$ is the group-delay-compensated results of 200-order FIR filter with 500 Hz cut-off frequency. As shown in Fig. 23, the noise RSSEs of u_d^* are 5.49, 11.1, 21.0, and 11.1 for those four cases. The results indicate that the noise suppression

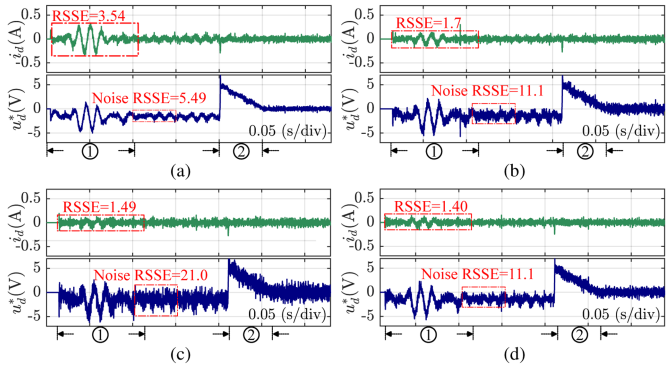

Fig. 23. In the first phase, the secondary operates at a nominal speed of 1 m/s, and the focus is on suppressing a back-EMF disturbance that occurs when $\theta_e \in \mathcal{P}$. In the second phase, the secondary is decelerated to zero speed with maximum acceleration, which is another typical operation condition of PMLSM. The traditional RPCC with $\omega_{oc} = 1k$, $2k$ and $3k$ rad/s is used in (a), (b), and (c), respectively. The modified RPCC is used with $\omega_{oc} = 3k$ rad/s, $R_{da} = R'_s$ and $\alpha = 0.6$ in (d).

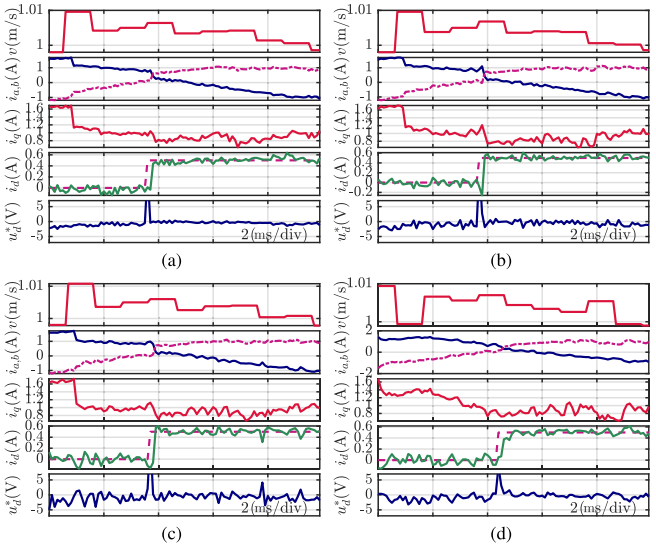

Fig. 24. A step current with 0.5 A is injected in i_d for step response test in 1 m/s speed operation. Traditional robust DPCCs with $\omega_{oc} = 1000$, 2000, and 3000 rad/s are used in (a), (b), and (c), respectively. Modified RPCC with $\omega_{oc} = 3k$ rad/s, $R_{da} = R'_s$ and $\alpha = 0.6$ is employed in (d).

performance of the improved RPCC algorithm is comparable to that of the robust DPCC with $\omega_{oc} = 2000$ rad/s, but with better disturbance suppression performance. These results align with the theoretical analysis presented in Figs. 9 and 11.

The experiment results for the current step response at the rated speed point are presented in Fig. 24. The robust DPCC can track the reference within two control cycles without overshooting, regardless of the value of ω_{oc}. This indicates nearly perfect reference tracking performance, consistent with the theoretical analysis in Section III-B and the frequency sweep experimental results depicted in Fig. 19. That is to say, in the absence of parameter mismatch, the internal equivalent integrator of the LESO does not affect the rapid reference tracking of the robust DPCC.

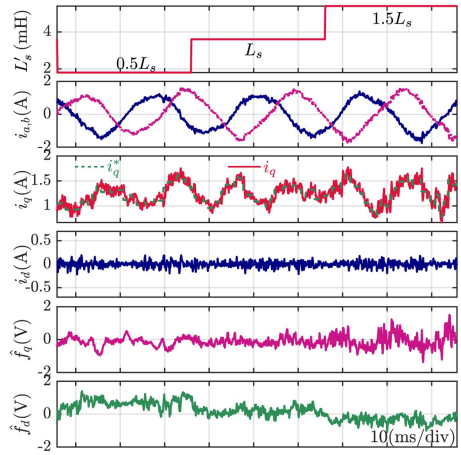

Fig. 25. Response of the modified RPCC with $\omega_{oc} = 3k$ rad/s, $R_{da} = R'_s$, and $\alpha = 0.6$ under inductance parameter mismatch and $v = 1$ m/s.

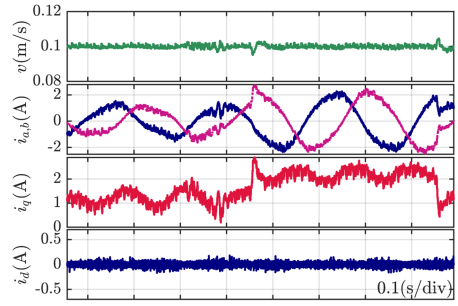

Fig. 26. Response of the modified RPCC with $\omega_{oc} = 3k$ rad/s, $R_{da} = R'_s$, and $\alpha = 0.6$ when 16 N load is added to the secondary with 0.1 m/s. The speed controller adopts a two-degree PI controller in [30], and the desired speed-loop bandwidth is set as 200 rad/s.

The reference tracking performance of the improved RPCC is slightly weaker, with a settling time of $5T_s$ and no overshoot. This characteristic is consistent with the theoretical analysis results in Fig. 10 and the frequency sweep experimental results in Fig. 20(b). However, as can be seen from the speed fluctuations in Fig. 24, the deviation between the current reference tracking bandwidths of 1 and 2 kHz does not significantly impact the outer loop. Pursuing excellence in a single performance metric is inappropriate. Under the constraints of fundamental lower limits, it is more meaningful to seek simultaneous optimization of multiple performance metrics.

The parameter robustness of the improved RPCC is illustrated in Fig. 25. It can be observed that at the rated speed operating point when the control parameter L'_s varies from $0.5L_s$ to $1.5L_s$, the current closed-loop system remains stable and exhibits good steady-state tracking accuracy and noise suppression performance. The GM demonstrated in Fig. 25 is consistent with the theoretical derivation results in Section IV. As shown in Fig. 10, the improved RPCC has $\overline{\sigma}[\boldsymbol{S}(\omega_s)] < 2$.

Finally, a low-speed loading experiment is conducted, and the results are presented in Fig. 26. Under a sudden increase and decrease of 16 N load, the maximum speed fluctuation of the secondary is 5 %, with a recovery time of 12 ms. Under constant load or no-load conditions, the servo system suppresses the influence of PMLSM detent force, limiting the speed ripple to within 2 %. This demonstrates that the driver can achieve excellent outer loop control performance based on the proposed improved RPCC current control algorithm.

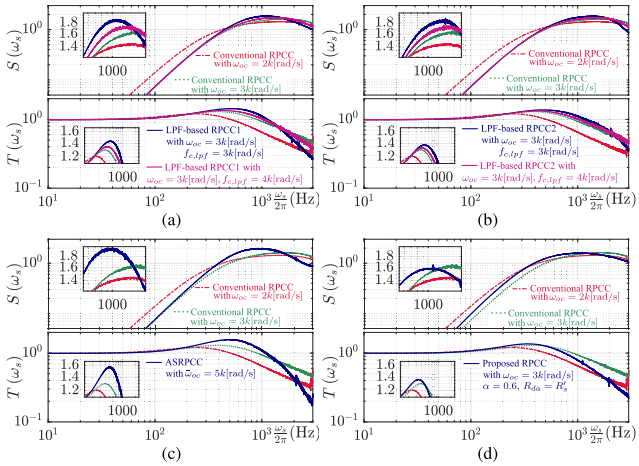

Fig. 27. Sweep-frequency results of different noise-immunity-enhanced RPCC compared with the conventional RPCC. (a) LPF-based RPCC1; (b) LPF-based RPCC2; (c) ASRPCC; (d) Proposed RPCC. Those frequency responses are processed by a zero-phase filter.

D. Further Discussion

A set of sweep frequency experiments are conducted to verify the correctness of the analysis for the three existing noise-immunity-enhanced RPCCs shown in Fig. 13 in Section IV-B. The sweep frequency method is the same as in Fig. 18. The results are shown in Fig. 27. The frequency response of the current closed-loop system obtained from the sweep frequency experiments is consistent with the theoretical analysis results shown in Fig. 14. In Fig. 27(a) and (b), the parameters ω_{oc} of LPF-based RPCC1 and RPCC2 are set to 3000 rad/s so that the disturbance rejection performance at mid frequencies is the same as that of the traditional RPCC with $\omega_{oc} = 3000$ rad/s. Under the constraint of stability margin ($M_S < 2$, $M_T \leq 1.4$), the cutoff frequency of the filters $f_{c,\text{lpf}} > 3$ kHz for both noise-immunity-enhanced RPCCs. Compared with the traditional RPCC, the filters bring phase lag, increasing M_T, which in turn causes the noise suppression performance at high frequencies from 1 to 3 kHz to be weaker than that of the traditional RPCC with $\omega_{oc} = 2k$ rad/s.

In Fig. 27(c), the disturbance rejection performance of ASRPCC with $\bar{\omega}_{oc} = 5k$ rad/s at mid frequencies is the same as that of the traditional RPCC with $\omega_{oc} = 3000$ rad/s, and its noise suppression performance at frequencies $\omega_s > 2$ kHz is stronger than that of the traditional RPCC and the proposed RPCC shown by the navy waveform in Fig. 27(d). However, consistent with the theoretical analysis results shown in Fig. 14, the stability margin of ASRPCC significantly decreases, with $M_S \approx 2$ and $M_T \approx 1.6$, and its noise suppression performance in the frequency range of 200 Hz–1 kHz is significantly weaker than that of other RPCCs.

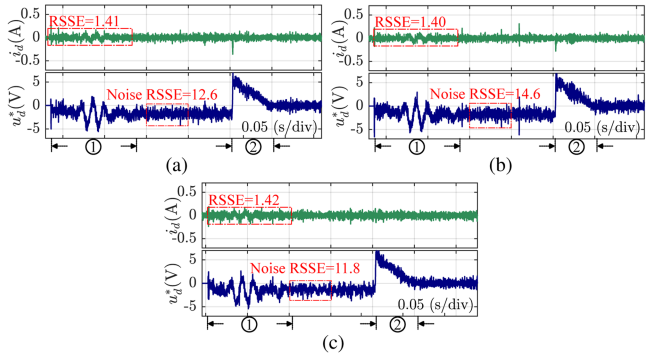

Fig. 28. d-axis current response and voltage command of different existing noise-immunity-enhanced RPCC for $\theta_e \in \mathcal{P}$ at 1 m/s. (a) LPF-based RPCC1 with $\omega_{oc} = 3k$ rad/s, $f_{c,lpf} = 3k$ Hz; (b) LPF-based RPCC2 with $\omega_{oc} = 3k$ rad/s, $f_{c,lpf} = 3k$ Hz; (c) ASRPCC with $\bar{\omega}_{oc} = 5k$ rad/s.

Finally, the frequency response shown in Fig. 27(d) again demonstrates the optimal comprehensive performance of the proposed improved RPCC regarding stability margin, disturbance rejection, and noise immunity.

The conclusions obtained from the sweep frequency experiments are further validated in the time-domain response experiments shown in Fig. 28. The current tracking accuracy of the three existing noise-immunity-enhanced RPCCs during the $\theta_e \in \mathcal{P}$ phase is comparable to that of the improved RPCC shown in Fig. 23(d) and the traditional RPCC with $\omega_{oc} = 3000$ rad/s shown in Fig. 23(c). However, their noise suppression performance is inferior to the proposed RPCC.

VI. Conclusion

This article proposes an improved RPCC for WDS-PMLSM. The improved algorithm ensures larger 1 kHz bandwidth for command tracking and simultaneously enhances noise suppression and disturbance rejection performance while maintaining appropriate stability margins ($\overline{\sigma}[\boldsymbol{S}(\omega_s)] < 2$). When $\theta_e \in \mathcal{P}$, under the same noise suppression performance, the RSSE of current tracking for the improved algorithm is 1.4, while for the traditional robust DPCC, it is 1.7. Compared with three existing noise-immunity-enhanced RPCCs, the proposed scheme shows optimal comprehensive performance in terms of stability margin, disturbance suppression, and noise immunity. These performances are investigated by an improved analysis method for closed-loop MIMO systems.

References

[1] Q. Sun, M. Wang, M. Liu, C. Zhang, and L. Li, "Magnetic field distortion analysis and suppression for the minimum unit winding segmented moving-magnet linear motor," *IEEE Trans. Ind. Electron.*, vol. 71, no. 4, pp. 3452–3460, Apr. 2024.

[2] T. Zhang, X. Mei, and X. Du, "A new winding segmented permanent magnet linear synchronous motor for multiple passive carriers," *IEEE Trans. Magn.*, vol. 58, no. 7, Jul. 2022, Art. no. 8202309.

[3] B. Xiang, T. Wen, and H. Liu, "Cooperative control of multiple pm actuators in pmlsm with segmented windings," *IEEE Trans. Transp. Electrific.*, vol. 10, no. 3, pp. 5570–5580, Sep. 2024, doi: 10.1109/TTE.2023.3327047.

[4] K. Guo et al., "A phase-domain model of dual three-phase segmented powered linear pmsm for hardware-assisted real-time simulation," *IEEE Trans. Ind. Appl.*, vol. 58, no. 4, pp. 4511–4521, Jul./Aug. 2022.

[5] M. Wang, K. Kang, C. Zhang, and L. Li, "A driver and control method for primary stator discontinuous segmented-pmlsm," *Symmetry*, vol. 13, no. 11, 2021, Art. no. 2216.

[6] S. Silaghiu and P. Mutschler, "Monitoring and control of a modular servo drive system based on pm linear synchronous motors," in *Proc. 36th Annu. Conf. IEEE Ind. Electron. Soc.*, 2010, pp. 906–911.

[7] F. Yang, X. Zhao, H. Jin, X. Wang, and X. Liu, "Improved deadbeat predictive current control with embedded resonant polynomial and disturbance observer for pmsm current distortion rejection," *IEEE J. Emerg. Sel. Topics Power Electron.*, vol. 12, no. 2, pp. 1934–1945, Apr. 2024.

[8] Z. Hao, Y. Yang, K. Shao, and Y. Liu, "Switching active disturbance rejection based deadbeat predictive current control for permanent magnet synchronous motors," *IEEE Trans. Power Electron.*, vol. 38, no. 11, pp. 13920–13932, Nov. 2023.

[9] C. Gong, L. Ding, Y. Li, X. Wu, and X. Zhang, "Flux observation transfer-based inductance identification technique for precise fcs-mpcc used in surface-mounted pmsms," *IEEE Trans. Power Electron.*, vol. 38, no. 4, pp. 4241–4245, Apr. 2023.

[10] Y. Wang et al., "A robust dpcc for ipmsm based on a full parameter identification method," *IEEE Trans. Ind. Electron.*, vol. 70, no. 8, pp. 7695–7705, Aug. 2023.

[11] F. Wang, L. He, J. Kang, R. Kennel, and J. Rodríguez, "Adaptive model predictive current control for pmlsm drive system," *IEEE Trans. Ind. Electron.*, vol. 70, no. 4, pp. 3493–3502, Apr. 2023.

[12] M. Hu, W. Hua, C. Cheng, Y. Wang, and C. Lu, "Discrete-time frequency-domain disturbance observer to mitigate harmonic current in pmsm drives and the implementation with reduced delay," *IEEE Trans. Power Electron.*, vol. 38, no. 8, pp. 9482–9493, Aug. 2023.

[13] F. Wang, D. Ke, X. Yu, and D. Huang, "Enhanced predictive model based deadbeat control for pmsm drives using exponential extended state observer," *IEEE Trans. Ind. Electron.*, vol. 69, no. 3, pp. 2357–2369, Mar. 2022.

[14] B. Wang, X. Chen, Y. Yu, G. Wang, and D. Xu, "Robust predictive current control with online disturbance estimation for induction machine drives," *IEEE Trans. Power Electron.*, vol. 32, no. 6, pp. 4663–4674, Jun. 2017.

[15] M. Hu, W. Hua, Z. Wang, S. Li, P. Wang, and Y. Wang, "Selective periodic disturbance elimination using extended harmonic state observer for smooth speed control in pmsm drives," *IEEE Trans. Power Electron.*, vol. 37, no. 11, pp. 13288–13298, Nov. 2022.

[16] T. Li, X. Sun, M. Yao, D. Guo, and Y. Sun, "Improved finite control set model predictive current control for permanent magnet synchronous motor with sliding mode observer," *IEEE Trans. Transp. Electrific.*, vol. 10, no. 1, pp. 699–710, Mar. 2024.

[17] Y. Yan, Z. Sun, J. Yang, and S. Li, "A guide for gain tuning of disturbance observer: Balancing disturbance estimation and noise suppression," in *Proc. 2018 IEEE Conf. Control Technol. Appl.*, 2018, pp. 1558–1563.

[18] D. Astolfi, M. Jungers, and L. Zaccarian, "Output injection filtering redesign in high-gain observers," in *Proc. 2018 Eur. Control Conf.*, 2018, pp. 1957–1962.

[19] Y. Zuo, J. Mei, C. Jiang, X. Yuan, S. Xie, and C. H. Lee, "Linear active disturbance rejection controllers for pmsm speed regulation system considering the speed filter," *IEEE Trans. Power Electron.*, vol. 36, no. 12, pp. 14579–14592, Dec. 2021.

[20] Q. Hou et al., "Enhanced active disturbance rejection control with measurement noise suppression for pmsm drives via augmented nonlinear extended state observer," *IEEE Trans. Energy Convers.*, vol. 39, no. 1, pp. 287–299, Mar. 2024.

[21] Z. Lin, X. Ruan, H. Zhang, and L. Wu, "A generalized real-time computation method with dual-sampling mode to eliminate the computation delay in digitally controlled inverters," *IEEE Trans. Power Electron.*, vol. 37, no. 5, pp. 5186–5195, May 2022.

[22] M. Hu et al., "Fast current control without computational delay by minimizing update latency," *IEEE Trans. Power Electron.*, vol. 36, no. 11, pp. 12207–12212, Nov. 2021.

[23] Q. Tan, X. Huang, L. Li, and M. Wang, "Research on inductance unbalance and thrust ripple suppression of slot-less tubular permanent magnet synchronous linear motor," *IEEE Access*, vol. 6, pp. 51011–51020, 2018.

[24] M. Ma, L. Li, J. Zhang, J. Yu, and H. Zhang, "Investigation of cross-coupling inductances for long-stator pm linear motor arranged in multiple segments," *IEEE Trans. Magn.*, vol. 51, no. 11, Nov. 2015, Art. no. 8205304.

[25] J. Han, "From pid to active disturbance rejection control," *IEEE Trans. Ind. Electron.*, vol. 56, no. 3, pp. 900–906, Mar. 2009.
[26] M. Yang, X. Lang, J. Long, and D. Xu, "Flux immunity robust predictive current control with incremental model and extended state observer for pmsm drive," *IEEE Trans. Power Electron.*, vol. 32, no. 12, pp. 9267–9279, Dec. 2017.
[27] S. Skogestad and I. Postlethwaite, *Multivariable Feedback Control: Analysis and Design*. Hoboken, NJ, USA: Wiley, 2005.
[28] C.-T. Chen, *Linear System Theory and Design*. Philadelphia, PA, USA: Saunders College Publishing, 1984.
[29] X. Wang, C. Jiang, F. Zhuang, C. H. Lee, and C. Chan, "A harmonic injection method equivalent to the resonant controller for speed ripple reduction of pmsm," *IEEE Trans. Ind. Electron.*, vol. 69, no. 10, pp. 9793–9803, Oct. 2022.
[30] L. Harnefors, S. E. Saarakkala, and M. Hinkkanen, "Speed control of electrical drives using classical control methods," *IEEE Trans. Ind. Appl.*, vol. 49, no. 2, pp. 889–898, Mar./Apr. 2013.

Anpeng Wang was born in Jiang Su, China, in 1996. He received the B.E. degree in electrical engineering form Nanjing Normal University, Nanjing, China, in 2018, and the M.E. degree in electrical engineering from Nanjing University of Aeronautics and Astronautics, Nanjing, China, in 2021. He is currently toward the Ph.D. degree in electrical engineering with the School of Electrical Engineering and Automation from Harbin Institute of Technology, Harbin, China.

His research interests include permanent magnet linear synchronous motors and the drive and control.

Liyi Li (Senior Member, IEEE) was born in Hei Longjiang, China, in 1969. He received the B.E. degree in precision instrument, the M.E. degree in machinery manufacturing and automation, and the D.E. degree in electrical engineering from Harbin Institute of Technology (HIT), Harbin, China, in 1991, 1995, and 2001, respectively.

Since 2004, he has been a Professor with the School of Electrical Engineering and Automation, HIT. He has authored or coauthored more than 110 technical papers, and holds 50 patents. His research interests include in control and drive of high-speed permanent magnet synchronous motors and linear motors.

Xuzhen Huang (Member, IEEE) received the B.E., M.E., and Ph.D. degrees in electrical engineering from the Harbin Institute of Technology, Harbin, China, in 2006, 2008, and 2012, respectively.

She is currently with the Nanjing University of Aeronautics and Astronautics, Nanjing, China, where she is a Professor of electrical engineering. Her research interests include the linear permanent magnet synchronous motors and the thermal analysis of motors.